Received: 27 July 2021 | Revised: 1 March 2022 | Accepted: 2 March 2022 | Published on: 22 March 2022

DOI: 10.1002/mrm.29243

RESEARCH ARTICLE

Magnetic Resonance in Medicine

Short TE downfield magnetic resonance spectroscopy in a mouse model of brain glioma

Sónia I. Gonçalves | **Rui V. Simões** | **Noam Shemesh**

Champalimaud Research, Champalimaud Foundation, Lisbon, Portugal

Correspondence
Noam Shemesh, Champalimaud Research, Champalimaud Foundation, Av. Brasilia 1400-038, Lisbon, Portugal
Email: noam.shemesh@neuro.fchampalimaud.org;
Twitter: @ShemeshL

Funding information
Champalimaud Centre for the Unknown; CONGENTO; European Regional Development Fund (ERDF); European Research Council (ERC), Grant/Award Number: 679058; Fundação para a Ciência e Tecnologia, Grant/Award Number: LISBOA-01-0145-FEDER-022170; H2020 Marie Skłodowska-Curie Actions, Grant/Award Number: H2020-MSCA-IF-2018; Lisboa Regional Operational Programme

Purpose: Enhanced cell proliferation in tumors can be associated with altered metabolic profiles and dramatic microenvironmental changes. Downfield magnetic resonance spectroscopy (MRS) has received increasing attention due to its ability to report on labile resonances of molecules not easily detected in upfield ^{1}H MRS. Image-selected-in-vivo-spectroscopy-relaxation enhanced MRS (iRE-MRS) was recently introduced for acquiring short echo-time (TE) spectra. Here, iRE-MRS was used to investigate in-vivo downfield spectra in glioma-bearing mice.

Methods: Experiments were performed in vivo in an immunocompetent glioma mouse model at 9.4 T using a cryogenic coil. iRE-MRS spectra were acquired in $N = 6$ glioma-bearing mice (voxel size = 2.2^3 mm^3) and $N = 6$ control mice. Spectra were modeled by a sum of Lorentzian peaks simulating known downfield resonances, and differences between controls and tumors were quantified using relative peak areas.

Results: Short TE tumor spectra exhibited large qualitative differences compared to control spectra. Most peaks appeared modulated, with strong attenuation of NAA (~7.82, 7.86 ppm) and changes in relative peak areas between 6.75 and 8.49 ppm. Peak areas tended to be smaller for $DF_{6.83}$, $DF_{7.60}$, $DF_{8.18}$ and NAA; and larger for $DF_{7.95}$ and $DF_{8.24}$. Differences were also detected in signals resonating above 8.5 ppm, assumed to arise from NAD+.

Conclusions: In-vivo downfield ^{1}H iRE-MRS of mouse glioma revealed differences between controls and tumor bearing mice, including in metabolites which are not easily detectable in the more commonly investigated upfield spectrum. These findings motivate future downfield MRS investigations exploring pH and exchange contributions to these differences.

KEYWORDS
Magnetic Resonance Spectroscopy, MRS, Glioma, iRE-MRS, Downfield, Mouse

1 | INTRODUCTION

Gliomas are the most common infiltrative neoplasm of the central nervous system,[1] representing approximately 40%[2] of all diagnosed central nervous system tumors. Glioblastomas are the most aggressive and frequent type of glioma and are usually histologically classified as grade

© 2022 International Society for Magnetic Resonance in Medicine

15222594, 2022, 2, Downloaded from https://onlinelibrary.wiley.com/doi/10.1002/mrm.29243 by Cochrane Portugal, Wiley Online Library on [18/11/2022]. See the Terms and Conditions (https://onlinelibrary.wiley.com/terms-and-conditions) on Wiley Online Library for rules of use; OA articles are governed by the applicable Creative Commons License

IV.[3] Glioblastomas are typically heterogeneous, combining regions of e.g. necrosis, active proliferation, inflammation, infiltration, and neoangiogenesis,[4,5] which can produce different metabolic patterns compared to normal tissues.[6-8] Hence, non-invasive MRI methods[9,10] are pivotal in brain tumor diagnosis and management, especially in their initial detection, identification of infiltration margins, grade determination and recurrence detection.

One promising class of MRI experiments for noninvasively detecting and characterizing tumors involves chemical exchange saturation transfer (CEST)-based methods, which rely on exchange of labile resonances (resonating downfield of water) and water. For example, amide proton transfer (APT) and CEST[11,12] focusing on Glutamate (Glu) and Glutamine (Gln)[13,14] downfield resonances, were found to be useful for predicting tumor histological grade,[15] while other methods targeting regional variations in pH delineated tumor regions from peritumoral edema more accurately than, e.g., Gd contrast-enhanced MRI.[16,17] Such CEST or APT methods utilize the resonances from highly relevant chemical functional groups such as hydroxyls, amines, amides, aldehydes, aromatic, and carboxylic protons, amongst others,[18] which can be present in relatively high concentrations in vivo, in substances such as phenylalanine, homocarnosine (hCs), adenosine triphosphate, nicotinamide adenine dinucleotide (NAD^+) or glutathione. Given that CEST or APT methods have a very limited spectral resolution, which is typically traded off for spatial resolution, a more comprehensive characterization of downfield resonances in tumors could assist in the interpretation of such experiments.

^{1}H magnetic resonance spectroscopy (^{1}H MRS) can quantify more abundant (~mM) brain metabolites[19] with high spectral resolution and typically focuses on the spectral region upfield of the H_2O resonance, containing signatures of e.g. non-oxygenated aliphatic protons, aliphatic/aromatic acetoxyl protons, as well as methoxy protons.[20] Only a few studies with high dynamic range MRS[21-24] or relaxation-enhanced MRS (RE-MRS),[25] focused on downfield spectra,[26] and revealed (i) resonances undetectable in the upfield counterpart, such as the (tentatively assigned) NAD^+[27,28] and hCs resonances,[19] and (ii) exchange-related phenomena.[24] A few recent studies have extended the characterization of the downfield spectrum by measuring T1 and T2 relaxation times, exchange rates, and metabolite concentration.[29,30] The pH sensitivity of the downfield spectrum has been explored by using the modulation of downfield peaks for pH estimation and peak assignment.[31] The robustness in the quantification of (tentatively assigned) NAD+ in healthy volunteers has been shown,[32] allowing the demonstration of the negative correlation between NAD+ concentration and age. Finally, recently it has been shown that magnetic resonance spectroscopic imaging can reliably map downfield resonances in the human brain at 3 T.[33]

Image-selected-in-vivo-spectroscopy (ISIS) RE-MRS (iRE-MRS),[34] combines RE-MRS[25] with ISIS localization[35] to record spectra with short TEs (~5 ms), enabling the characterization of broad signals in the downfield spectrum. iRE-MRS principles have since been extended to the human brain,[36,37] yielding similar downfield spectra to those presented by Gonçalves et al.[34] in rat brains. Given that brain tumors can involve modified metabolic concentrations and/or exchange properties (e.g. due to pH), we here aimed to harness iRE-MRS to investigate in-vivo downfield MRS spectra in a mouse glioma model. We find intriguing differences in downfield spectra in gliomas as compared to healthy controls, suggesting a potential role for downfield MRS in tumor characterization.

2 | METHODS

All animal experiments were carried out in agreement with the EU Directive 2010/63, and were preapproved by the Champalimaud Animal Welfare Body and the national competent authority (Direcção Geral de Alimentação e Veterinária, DGAV).

2.1 | Animal housing and preparation

Experiments were carried out on wild-type mice, $N = 6$ controls (4 males, mean weight = 21.5 ± 1.2 g) and $N = 6$ tumors (2 males, mean weight = 21.2 ± 1.6 g), aged ~8–11 weeks. The animals were housed in a 12-h light/-dark cycle, up to 5 per cage, with food and water provided ad libitum. Tumors were induced in all $N = 6$ animals by intracranial stereotactic injection of 10^5 GL261 cells in the caudate nucleus as previously reported in Ref.38. Briefly, animals were immobilized on a stereotactic holder under 1–2% isoflurane anesthesia. The skull was exposed and a 1 mm hole was drilled, 2.32 mm lateral right to the midline and 0.1 mm caudal to the bregma. A 26G syringe on a digital push-pull microinjector was inserted into the striatum, at 2.35 mm from the cortical surface, and 4 μL of PBS containing the GL261 cells was injected at a rate of 2 μL/min. The syringe was slowly removed 2 min after the injection finished. The incision site was closed with suture silk (5/0), and the animal was placed in a warm environment for recovery. Analgesia was also administered: meloxicam (1.0 mg/kg s.c.), 30 min prior to intervention and every 24 h during the following 2 days; buprenorphine (0.05 mg/kg s.c.), once the animal started to recover from anesthesia.

15222594, 2022, 2, Downloaded from https://onlinelibrary.wiley.com/doi/10.1002/mrm.29243 by Cochrane Portugal, Wiley Online Library on [18/11/2022]. See the Terms and Conditions (https://onlinelibrary.wiley.com/terms-and-conditions) on Wiley Online Library for rules of use; OA articles are governed by the applicable Creative Commons License

2.2 | Pulse sequence design

The iRE-MRS pulse sequence has been described in Gonçalves et al.[34] and is illustrated in Figure 1. It is based on spectrally-selective excitation and refocusing, avoiding water suppression. However, unlike the previous RE-MRS studies,[25,26] localization is achieved by an ISIS block, consisting of three spatially-selective adiabatic inversions, prior to the spin-echo sequence, which is repeated eight times to achieve three-dimensional localization. The refocusing pulse is surrounded by weak spoiler gradients along the three physical axis to remove unwanted coherence pathways and residual water signals. In addition, outer volume suppression (OVS) modules were implemented to improve localization accuracy.

2.3 | Spectrally-selective RF pulses

Spectrally-selective RF pulses were generated by the shape algorithm implemented in Paravision 6.0.1 (Bruker-Biospin, Ettlingen, Germany), which employs the Shinar-Le Roux algorithm.[39]

2.4 | MRS experiments

All experiments were performed on a 9.4 T horizontal bore scanner (Bruker Biospin, Karlsruhe, Germany) furnished with an AVANCE III HD console and with gradients producing up to 660 mT/m isotropically. An 86 mm quadrature resonator was used for excitation while a 4-element array surface cryocoil (for mouse head) (Bruker Biospin, Fallanden, Switzerland) was used for signal reception.

Experiments were carried out approximately 2.5 weeks after injection. Anesthesia was induced using ~5% isoflurane in approximately 20% O_2 and 80% air and maintained at 1–2% isoflurane for the entire scanning session. Temperature and breathing rate were constantly monitored and kept at 36–37° and 60–70 BPM respectively.

T2 RARE axial and coronal images were acquired for anatomical reference and voxel positioning with the following parameters: TR/TE = 2000/36 ms; 128×128 matrix; FOV = 16.1×16.1 mm; 0.126×0.126 mm in-plane resolution; slice thickness = 0.6 mm; 10 (15) slices in coronal (axial) view; 8 averages. iRE-MRS spectra were obtained from $2.2 \times 2.2 \times 2.2\,mm^3$ voxels located in the striatum, containing healthy brain parenchyma or tumor tissue. Both excitation and refocusing pulses were centered at 9.5 ppm, with 6.5 ppm bandwidth, residual water excitation of less than 6%. TR/TE = 15 000/5 ms, and 15 repetitions (each containing $N_{ISIS} = 8$ ISIS cycles), resulting in a total scan duration of 30 min. The spoiler gradient was set to 300 μs and 13.33% of the maximum gradient amplitude, 5597.01 Hz spectral width, and 1442 data points. Prior to ISIS localization, $N_{OVS} = 6$ OVS modules were executed to minimize outer-volume (OV) contamination. In addition, a long TR of 15 000 ms was used to allow for full relaxation, thus completely avoiding T1 smearing effects that could also lead to OV contamination originating from the ISIS module.[40] The water linewidth (full width half maximum in absorption mode) was measured from the water spectrum acquired with point resolved spectroscopy (PRESS) from the same voxel and with the same shim settings as iRE-MRS without apodization. Acquisition parameters were: TR/TE = 5000/16 ms, 1 repetition, 4807.69 Hz spectral width, 1442 data points.

2.5 | Data processing

Data processing was carried out using routines written in-house in Matlab® (Mathworks, Natick, MA). Each FID, resulting from summing over 8 ISIS cycles in 1 repetition, was Fourier transformed. The resulting spectrum was frequency and phase aligned using a non-linear least-squares procedure that respectively minimized the difference in magnitude and phase between each spectrum and the average.[41,42] The interval 6.5–8.5 ppm was taken as reference for the frequency alignment minimization procedure. The individually phase and frequency aligned spectra were averaged over the total number of repetitions in each scan. Apodization was carried out leading to a line broadening by 20 Hz. Each spectrum was baseline-corrected by cubic spline fitting with manually and individually chosen interpolation points (Figure S1 from Supporting Information)[43] and the spectra of different animals were manually aligned to the maximum of peak $DF_{6.83}$ (Figure 3). For qualitative evaluation of differences between groups, individual spectra were scaled (in the 6–16 ppm range) using unit length (UL2) normalization[44–47] before averaging over animals.

Unscaled individual spectra were modeled by a sum of Lorentzian functions simulating previously detected downfield peaks (Supporting Information Table S1)[29–31,48] and the fit was carried-out using a bounded least-squares minimization procedure. In total, the model fitted 42 parameters (14 chemical shifts, 14 peak widths and 14 peak heights), where peak chemical shifts were allowed to vary within 0.03 ppm around the nominal value to account for shifts due to e.g. B0 inhomogeneities and pH effects; peak widths were bounded between 0 and 1000 Hz; peak heights were bounded between 0 and the maximum peak height over all acquired spectra. Water spectra acquired with PRESS were fitted with a single Lorentzian function and water peak areas were calculated for all animals. Differences between groups were quantified by normalized

15222594, 2022, 2, Downloaded from https://onlinelibrary.wiley.com/doi/10.1002/mrm.29243 by Cochrane Portugal, Wiley Online Library on [18/11/2022]. See the Terms and Conditions (https://onlinelibrary.wiley.com/terms-and-conditions) on Wiley Online Library for rules of use; OA articles are governed by the applicable Creative Commons License

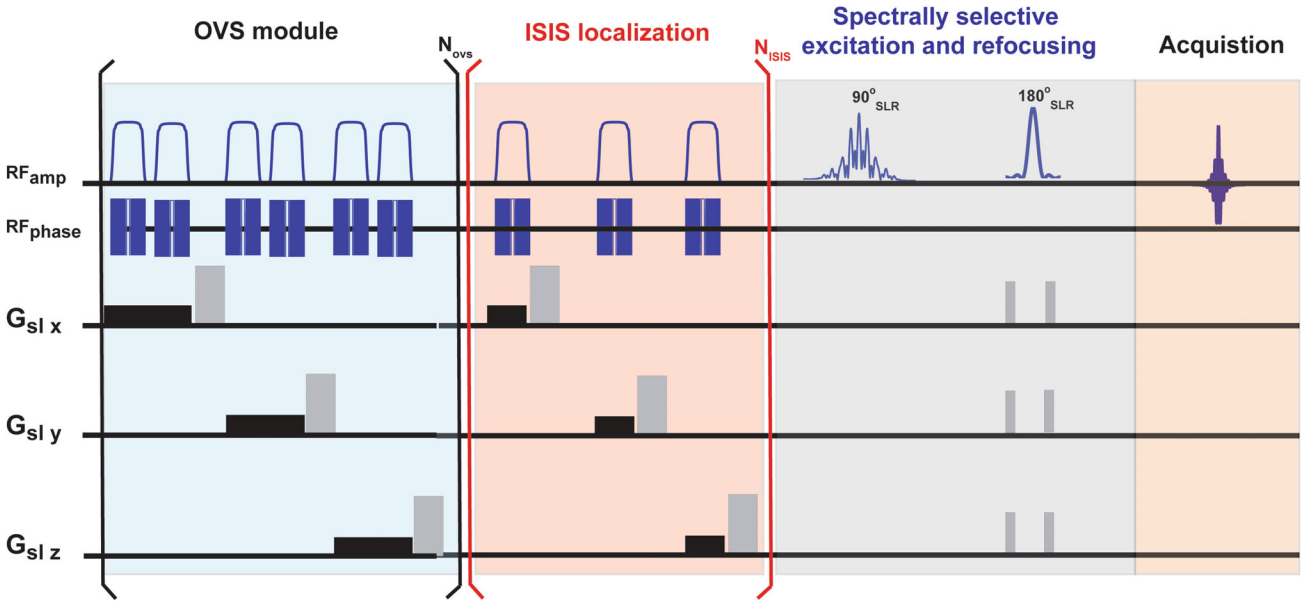

FIGURE 1 iRE-MRS Pulse sequence diagram. The RE-MRS, namely, the spectrally-selective excitation and refocusing pulses is followed by data acquisition, and preceded by an ISIS localization block that is repeated $N_{ISIS} = 8$ times for each scan, and by an OVS module that is repeated $N_{OVS} = 6$ times

metabolite peak areas with respect to the total downfield spectral area – m_{AD} – and to the water peak area – m_{AW}; their statistical significance (for $p < 0.05$) was tested using the Mann–Whitney U-test.

Tumor volumes were calculated from the reference T2 RARE images in axial and coronal views, as the average volume calculated from both anatomical views.

3 | RESULTS

Tumors were successfully induced and were clearly detectable in all mice 2–3 weeks after induction, mainly in the striatum (Figure 2 and Table 1). On T2-weighted anatomical images (Figure 2), the tumors appeared highly heterogeneous with regions of hypo- and hyper-intensity, likely associated with hemorrhage and edema, respectively. Tumor volumes were quite variable, ranging from 8 to 59 mm^3 (Table 1) at the time of the experiments.

Figure 3 depicts iRE spectra for two representative animals from the control group and two animals from the tumor group (c.f. Supporting Information Figures S2 and S3 for spectra from all other animals). Voxel definitions are shown in controls (A, C) and tumors (E, G) and the corresponding spectra are shown in (B, D) and (F, H), respectively. The control spectrum in the mouse brain is highly consistent with the main features reported previously in the rat brain.[34] The typical signal-to-noise ratio in these spectra, calculated for $DF_{8.24}$ in Figure 3, was 44.0 ± 12.1 for controls, and 52.0 ± 10.7 for tumors. The average water linewidth was 28.5 ± 9.3 Hz for tumors and 19.7 ± 2.9 Hz in controls. The differences in signal-to-noise ratio and average linewidth between groups did not reach a statistically significant threshold.

Although tumor downfield spectra exhibit somewhat higher variability, consistent resonances can be detected in all spectra. Figure 4 shows the average spectra over animals for controls and tumors, where the gray shaded area represents the standard deviation across animals. The average spectrum profile of the control mouse brain is again highly consistent with previous results in the rat[34] and humans,[29,30] and contains contributions from the signals identified in Borbath et al.[31] (Supporting Information Table S1). In particular, the smaller spectral peak in the 6.5–7.5 ppm range, identified as $DF_{7.10}$ (7.10 ppm), likely includes contributions from both hCs at 7.08 ppm (which also has a resonance at 8.08 ppm overshadowed by the broad $DF_{8.24}$ peak) and another unidentified component ($DF_{7.04}$) at 7.04 ppm[29–31]; NAA and "NAA broad" appear at 7.82 and 7.86 ppm respectively; $DF_{7.95}$ (7.95 ppm) appears as a small shoulder of the NAA peak; the H4, H6, and H2 protons, previously tentatively assigned to NAD^+, are just about visible at 8.85, 9.08 and 9.34 ppm[27,28,32]; $DF_{7.50}$ (7.50 ppm) containing signals from the unidentified component ($DF_{7.48}$) at 7.48 ppm[29–31] and from $DF_{7.60}$, tentatively assigned to amide protons of glutamine[48] (Supporting Information Table S1). Additionally, several other peaks (also previously reported[31,48]) are observed: $DF_{6.83}$ (tentatively assigned to glutamine at 6.83 ppm),

15222594, 2022, 2, Downloaded from https://onlinelibrary.wiley.com/doi/10.1002/mrm.29243 by Cochrane Portugal, Wiley Online Library on [18/11/2022]. See the Terms and Conditions (https://onlinelibrary.wiley.com/terms-and-conditions) on Wiley Online Library for rules of use; OA articles are governed by the applicable Creative Commons License

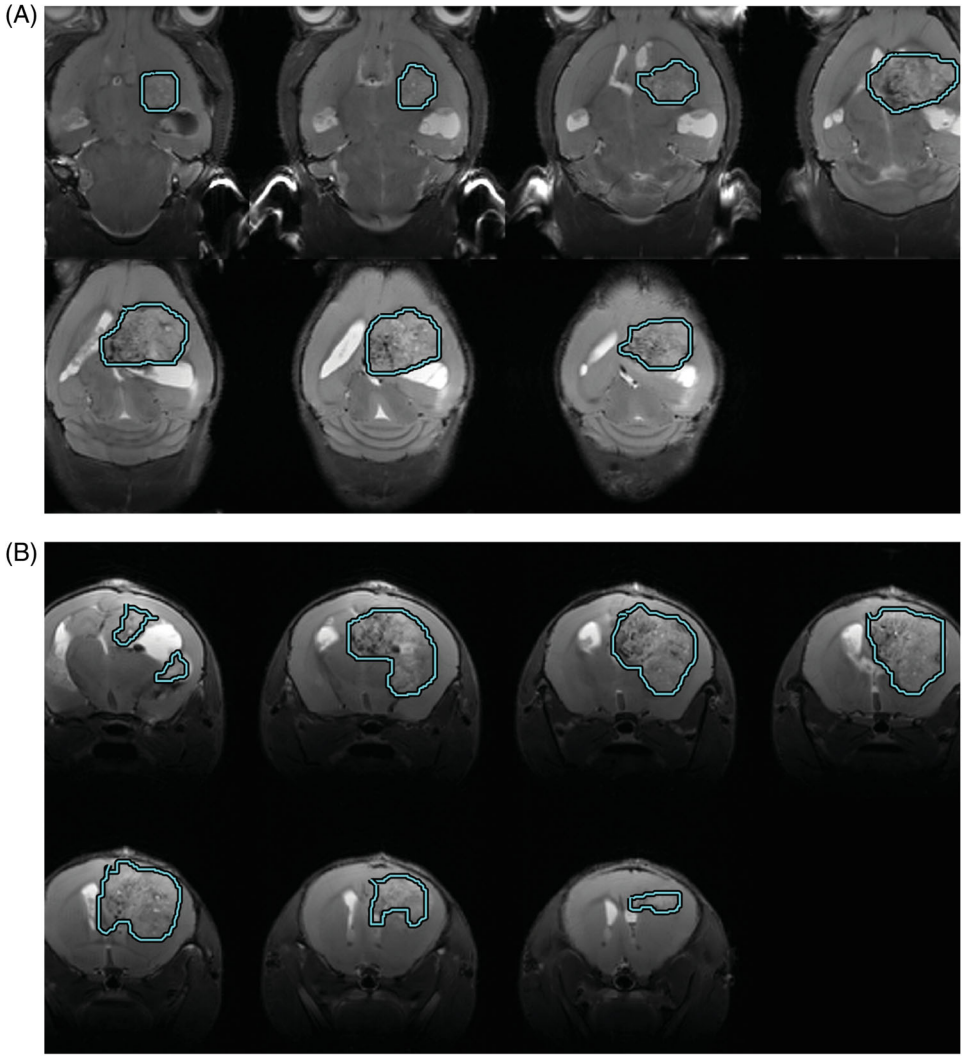

FIGURE 2 Tumor anatomy. Tumor appearance on reference T2-weighted anatomical images for a representative animal. (A) Coronal view. (B) Axial view. Notice the high heterogeneity of the tumor, with visible regions of hypo- and hyper-intensity. Tumors are delineated with a cyan line for visual clarity

$DF_{7.30}$ (7.30 ppm), $DF_{8.24}$ (8.00–8.40 ppm),[37] and $DF_{8.49}$ (8.49 ppm).

Interestingly, the average UL2 scaled tumor and control spectra show clear qualitative differences (Figure 4). For example, $DF_{6.83}$, $DF_{7.50}$ and $DF_{7.30}$ appear lower in the tumor group in this scaling. Furthermore, the peaks tentatively assigned to NAD+ are no longer detectable, though this observation remains tentative due to the very low signal-to-noise in these areas.

To better quantify these results, a simple model was fit to the unscaled individual spectra (Figure 5). Good agreement between model fit and measured data was noted, (c.f. the relatively small residuals for both groups). Figure 6 compares relative metabolite peak areas (m_{AD}) between the groups, where the entry NAA_T results from the sum of m_{AD} values for NAA and NAA broad. When compared to controls, relative peak areas in tumors tend to be smaller for $DF_{6.83}$ ($p = 0.06$), $DF_{7.60}$ ($p = 0.24$), NAA_T ($p = 0.002$), $DF_{8.18}$ ($p = 0.09$); and larger for $DF_{7.95}$ ($p = 0.03$), $DF_{8.24}$ ($p = 0.06$), hCs at 7.08 ppm ($p = 0.13$). Relative metabolite peak areas referenced to the area of the fitted water peaks (Supporting Information Figure S4) (m_{AW}) show a similar trend in tumors versus controls (Supporting Information Figure S5), but with lower statistical significance: smaller for $DF_{6.83}$ ($p = 0.24$), $DF_{7.60}$ ($p = 0.24$), NAA_T ($p = 0.002$),

TABLE 1 Tumor volumes. Calculated as the average tumor volume derived from axial and sagittal T2-RARE images. Note the large variability in tumor size

Animal	Tumor volume [mm^3]
1	51.7
2	59.5
3	34.4
4	8.6
5	24.4
6	12.6

15222594, 2022, 2, Downloaded from https://onlinelibrary.wiley.com/doi/10.1002/mrm.29243 by Cochrane Portugal, Wiley Online Library on [18/11/2022]. See the Terms and Conditions (https://onlinelibrary.wiley.com/terms-and-conditions) on Wiley Online Library for rules of use; OA articles are governed by the applicable Creative Commons License

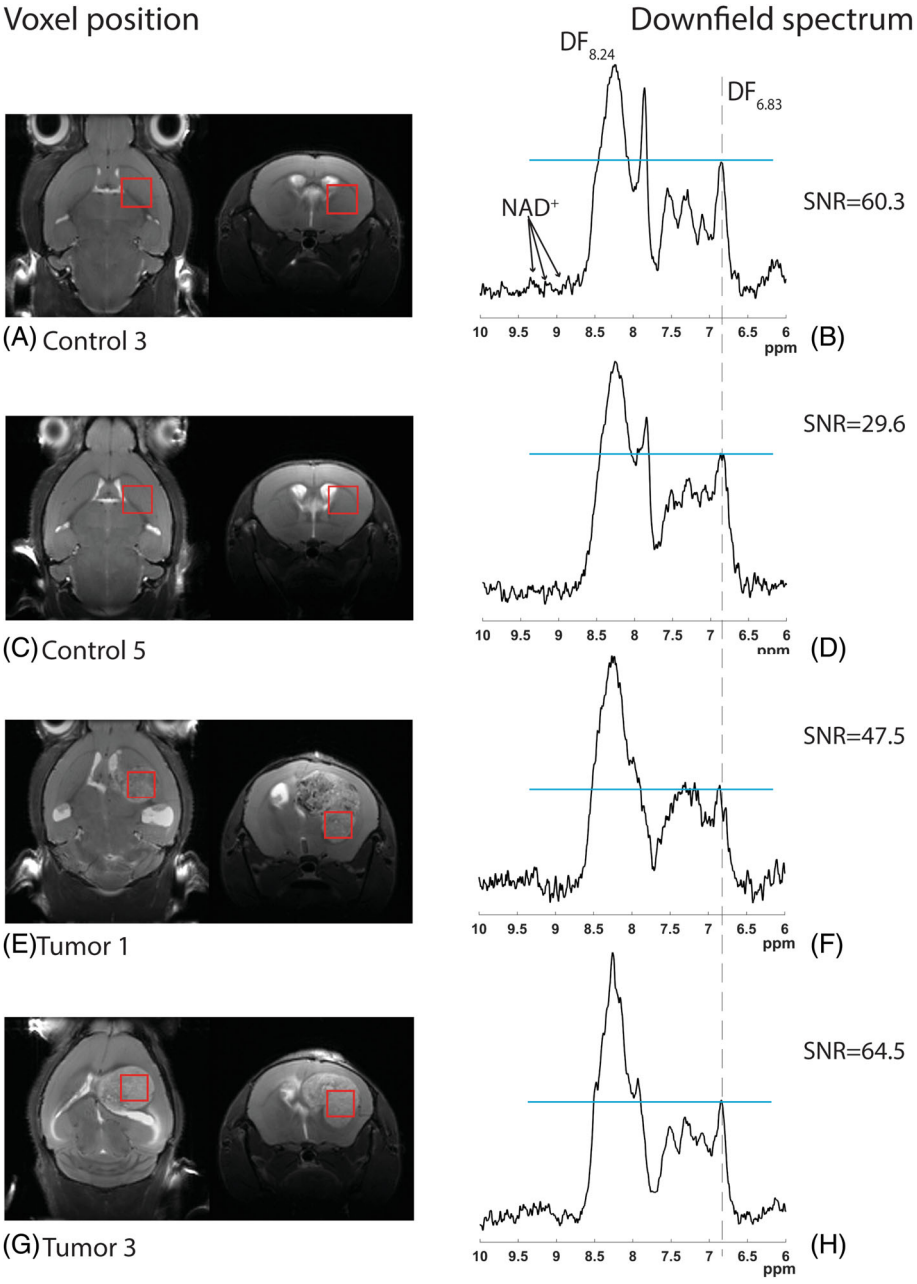

FIGURE 3 In vivo iRE-MRS at short TE. (A), (C) Voxel position in control mice. (B), (D) Representative downfield spectra in controls. (E), (G) Voxel position in tumor for two representative animals from the glioma group. (F), (H) Corresponding iRE-MRS downfield spectra in the tumor area. signal-to-noise ratio controls = 44.0 ± 12.1, signal-to-noise ratio tumors = 52.0 ± 10.7, calculated on peak $DF_{8.24}$. Vertical line identifies $DF_{6.83}$, used for inter-individual spectra alignment. Horizontal line marks the height of $DF_{6.83}$

$DF_{8.18}$ ($p = 0.18$); and larger for $DF_{7.95}$ ($p = 0.13$), $DF_{8.24}$ ($p = 0.48$), hCs at 7.08 ppm ($p = 0.18$).

4 | DISCUSSION

Magnetic resonance spectroscopy has been pivotal in investigating anatomical, functional, and metabolic properties of gliomas in vivo.[49–51] Most MRS and magnetic resonance spectroscopic imaging methods in tumors have insofar focused on the well characterized upfield resonances; still, recent evidence from CEST-based MRI measurements suggested that the areas resonating downfield of water could provide important and complementary information to that afforded by upfield signals. For example, GluCEST quantified the spatial distribution of Glu within different tumor regions,[52] showing the involvement of disturbed glutamate homeostasis in tumor aggressiveness and epileptogenicity, while APT imaging was proposed for tumor grading.[53] Still, APT and GluCEST are inherently limited by the relatively low spectral resolution, and their image contrast depends not only on metabolite concentration, but also on contributions from direct water saturation and magnetization transfer with semisolid tissue structures, as well as factors such as RF saturation power, B_0 heterogeneities and strength. Therefore, downfield MRS[21–34] could inform such measurements by investigating the downfield resonances with high

15222594, 2022, 2, Downloaded from https://onlinelibrary.wiley.com/doi/10.1002/mrm.29243 by Cochrane Portugal, Wiley Online Library on [18/11/2022]. See the Terms and Conditions (https://onlinelibrary.wiley.com/terms-and-conditions) on Wiley Online Library for rules of use; OA articles are governed by the applicable Creative Commons License

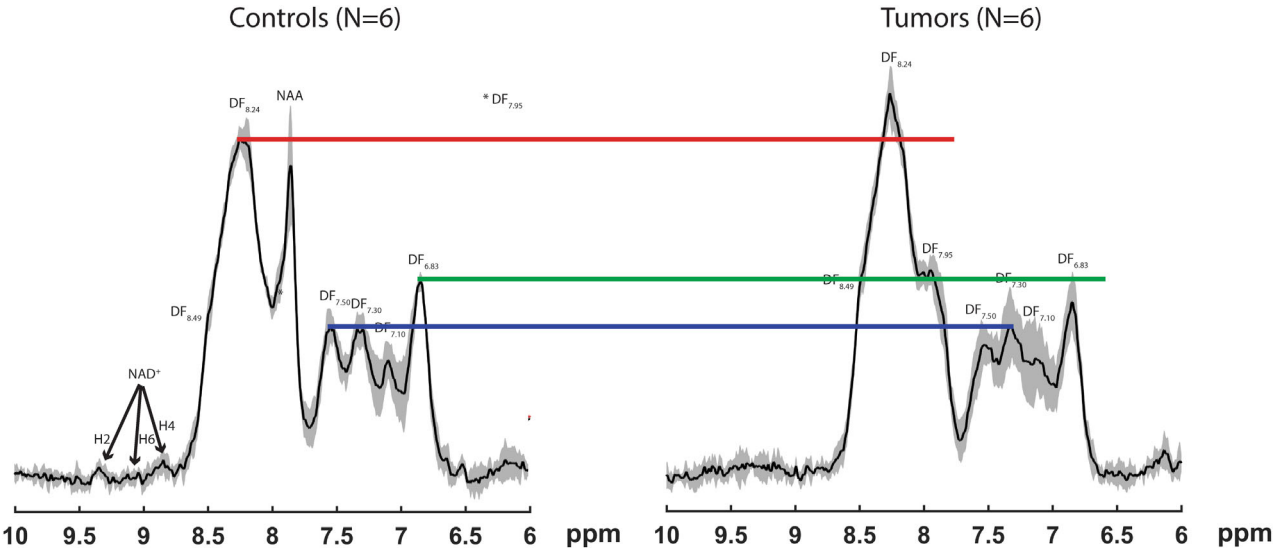

FIGURE 4 Average downfield iRE-MRS spectrum for controls and tumors (average over $N = 6$ animals). The average spectrum standard deviation over animals is represented as the gray shaded area. Main identified peaks: $DF_{6.83}$ (6.83 ppm), $DF_{7.10}$ (7.10 ppm), $DF_{7.30}$ (7.30 ppm), $DF_{7.50}$ (7.50 ppm), NAA/NAA broad, $DF_{7.95}$ (7.95 ppm), $DF_{8.24}$ (8.00–8.40 ppm), $DF_{8.49}$ (8.49 ppm), NAD+. Horizontal lines mark the height of $DF_{6.83}$, $DF_{7.50}$, and $DF_{8.24}$, for easy comparison with the tumor spectrum

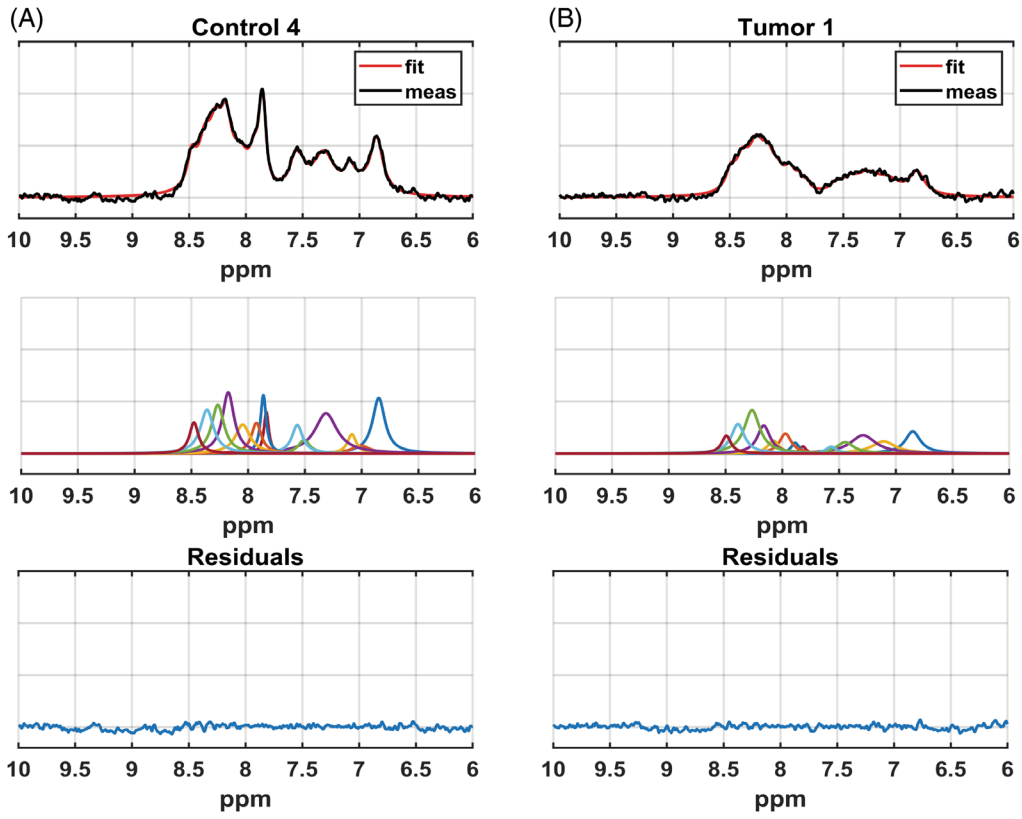

FIGURE 5 Model fit to individual spectra in two illustrative animals. (A) Control 4. (B) Tumor 1. Upper, middle and lower panels respectively represent measured versus fitted spectra, fitted peaks, and residuals

spectral resolution (at the expense of limited spatial resolution). Our study thus sought to characterize the downfield spectrum in glioma-bearing mice and investigate the spectral differences introduced by the tumors.

The recently developed short TE downfield spectroscopy (iRE-MRS) methodology was designed for better identifying broad downfield resonances and the relative relationships between the peaks, given the importance of

15222594, 2022, 2, Downloaded from https://onlinelibrary.wiley.com/doi/10.1002/mrm.29243 by Cochrane Portugal, Wiley Online Library on [18/11/2022]. See the Terms and Conditions (https://onlinelibrary.wiley.com/terms-and-conditions) on Wiley Online Library for rules of use; OA articles are governed by the applicable Creative Commons License

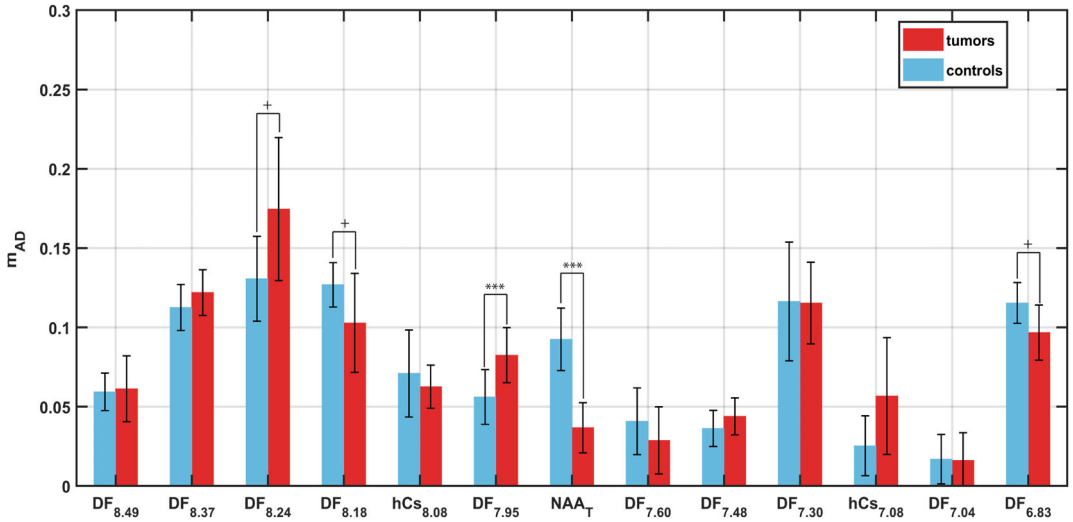

FIGURE 6 Relative metabolite peak areas (m_{AD}) calculated for individual spectra. Results for each spectral peak are presented as mean ± standard deviation calculated within each group. Statistically significant differences ($p < 0.05$) are marked with ***. Differences with $p < 0.1$ are marked with +

exchange/pH mechanisms in downfield signals. In this study, the iRE-MRS spectra were of sufficient spectral quality to qualitatively demonstrate changes in downfield spectra in tumors, although the relatively small cohort ($N = 6$) along with the inherent variability in tumor size and composition have prevented these trends from reaching statistical significance for most peaks. Still, the trends are visually apparent when inspecting individual spectra, thereby suggesting that with a larger cohort, this variability dimension may actually be very informative. In future studies, this variability could be minimized by changing the inclusion criteria from "time elapsed since tumor induction" to "stage of tumor growth", by minimizing the partial volume effects in tumor animals by using smaller voxels, and by extending the fit model. Nevertheless, given that downfield MRS has only been performed previously in healthy rats and in humans, our findings in this study have extended the scope of (short TE) downfield MRS towards the mouse – where many more animal models of pathology are available compared to other rodent models. Additionally it opens up the opportunity of characterizing changes in signals that do not have clear upfield signals, e.g., the previously-assigned NAD+ and hCs, in mouse models of disease.

Given the paucity of downfield MRS studies in healthy or diseased conditions, all the nomenclature and peak assignments in this study follow previous literature.[27–31] It is important to note that in the following discussion we consider some of these peaks as somewhat "tentatively" assigned, and stress that future studies should strive to further validate the identity of these signals. Another important aspect is the absence of a valid concentration standard, which might have contributed to the low statistical significance of the differences between groups for some peaks. Contrary to its upfield counterpart, downfield spectroscopic data depends not only on metabolite concentration, but also on pH and indirect magnetization transfer processes.[59] The pH of the tumor microenvironment is known to be more acidic than that of healthy tissue, which prevents the use of a comparable internal downfield reference for normalization of both tumor and control spectra. Likewise, the amount of water in tumor tissue is not only different from that in healthy tissue, but also quite variable from animal to animal (Supporting Information Figure S4), which makes water a questionable common internal reference for both controls and tumor animals. Therefore, any variations between controls and tumors should be interpreted as relative (to the total downfield spectral area or water signal) rather than absolute.

With these precautions in mind, it is worth considering the differences between tumor and control short TE spectra. In line with previous literature,[54] iRE-MRS clearly identified statistically significant decreases in N-acetylaspartate (NAA) amide signals (7.82, 7.86 ppm). Such decreases have been previously observed in upfield MRS signals acquired from glioblastoma tumors,[54] and likely reflect accelerated neuronal loss and/or shutdown of NAA synthesis.[55]

Beyond NAA, in tumors iRE-MRS identified a statistically significant increase of signals originating from the amide pool in proteins and peptides ($DF_{8.24}$). For peaks between 6.5 and 8 ppm, iRE-MRS identified a trend of decrease in $DF_{6.83}$ and $DF_{7.60}$, increase in hCs at 7.08 ppm, and a statistically significant increase in $DF_{7.95}$. It is interesting to consider which signals could contribute to the observed changes in these signals at such short TEs.

15222594, 2022, 2, Downloaded from https://onlinelibrary.wiley.com/doi/10.1002/mrm.29243 by Cochrane Portugal, Wiley Online Library on [18/11/2022]. See the Terms and Conditions (https://onlinelibrary.wiley.com/terms-and-conditions) on Wiley Online Library for rules of use; OA articles are governed by the applicable Creative Commons License

Multiple important metabolites and functional groups such as glutamine (6.82, 7.53 ppm), phenylalanine (7.30, 7.45 ppm), phosphocreatine (7.3 ppm), and amine groups from amino acids (7.5–7.7 ppm), such as glutamine or glutamate,[19] resonate in this spectral region. Glutamine contains two non-equivalent amide protons resonating at 6.82 and 7.53 ppm, which exchange with water at rates of the order of 10–30 Hz.[16] iRE-MRS at TE = 5 ms is expected to attenuate the glutamine signal by approximately 5–14%, due to exchange. Assuming a glutamine concentration in the 2–4 mM range[19] and 5–14% signal attenuation due to exchange, it is likely that measured peaks $DF_{6.83}$ and $DF_{7.50}$ contain contributions from the two glutamine amide protons. Amine protons on the other hand exchange with water at a much higher rate than amide protons (thousands of Hz vs tens of Hz, respectively).[16] For example, at TE = 5 ms and k = 1000 Hz, roughly 99% of the signal is expected to attenuate due to exchange. Decreasing TE to ~2 ms would have 10-fold increase of the remaining amine signal (to ~ 14% of the total signal), which would increase the likelihood of detection. Although a single TE experiment and the lack of a valid concentration reference makes the disambiguation of exchange/concentration changes more difficult, our findings are consistent with the decrease in glutamine/glutamate concentration in GL261 tumors when compared to controls reported in Doblas et al.[54] $DF_{7.95}$ (here tentatively assigned to the 7.95 ppm resonance of N-acetylaspartylglutamate (NAAG) as identified by de Graaf[43]) showed a statistically significant increase in tumors; we cannot exclude that this results from the contribution of another unidentified overlapping signal at short TEs, as NAAG signals are expected to decrease with NAA decreases.

Homocarnosines are another group of molecules whose signals are not typically detected in upfield spectra. The downfield resonances of the (tentatively assigned) hCs at 7.08 and 8.08 ppm have been identified in several human studies[29–31] but not in the rodent brain, where hCs concentration can be smaller. The in-vitro characterization of histidyl derivatives in the rat brain[56] suggests a concentration of hCs of the order of 0.5 mM, which we expect to be similar in the mouse brain. Furthermore, using a 2D-COSY approach, Braakman et al.[57] managed to resolve the GABA moiety of hCs in the upfield region of the spectrum in the in vivo mouse brain, suggesting that its concentration is sufficiently high for detection. The detected peak $DF_{7.10}$ potentially contains contributions from hCs at 7.08 ppm and from the unidentified 7.04 ppm component that was previously detected by Borbath et al.[31] In our data, the relative peak area of hCs at 7.08 ppm tends to be larger for tumors than for controls (though without reaching statistical significance) (Figure 6), which contrasts with a previous report on the concentration of hCs in glial tumors.[58] However, the average chemical shift of the Lorentzian peak simulating hCs at 7.08 ppm is 7.11 ppm in tumors, against 7.09 ppm in controls ($p = 0.06$), which may indicate a composite $DF_{7.10}$, containing contributions from other overlapping signal sources not currently included in the fitting model. Consequently, the larger relative peak area of hCs at 7.08 ppm could potentially originate from the increased contribution of unknown overlapping signal sources to the tumor spectra. In addition, this small shift suggests potential influences of other factors such as pH.[26,60] This is well demonstrated by the sensitivity of GluCEST to pH,[16,17] by the estimation of healthy brain tissue pH from the chemical shift of hCs spectral peaks at 7.08 and 8.08 ppm,[31] or by the dependence of peak $DF_{8.24}$ on both concentration and pH.[60–63] Therefore, one cannot exclude the influence of altered tumor pH on the chemical shift variation detected in tumor data, and in that case the increased relative peak area of the Lorentzian at 7.08 ppm would indeed originate from hCs. The sensitivity of the downfield spectrum to different pH and biochemical conditions of the tumor region,[64] could likely be teased apart – along with some of the spectral overlap inherent to broad signals[30] – using more sophisticated approaches involving multidimensional spectroscopy, signal modeling, multiple TEs, and saturation of different signals.

The tentative NAD+ H4, H6, and H2 resonances appear in the control spectrum (Figure 4) as three small peaks downfield of $DF_{8.49}$, similar to what has been previously found with iRE-MRS in the rat.[27,34] These difficult-to-detect resonances were not clearly observed in the average downfield spectrum of tumors, which to some extent disagrees with the more typical NAD+ increases expected from tumors.[65,66] However, the total amount of NAD+ in the tumor voxel results from a complex interplay of partial volume effects of the remaining neural tissue, cancer and stromal cells, necrosis, and edema areas. Even if cancer cells have increased metabolism, the loss of neural tissue (and concomitant decrease in NAD+) may be so profound that it overshadows the increase in NAD+ due to the tumor. A second hypothesis for the disappearance of these resonances in the tumor spectrum could be that they do not originate from NAD+, and further research should be carried out to reach a definite assignment for these three small peaks.

One limitation of this study is the voxel position within the tumor volumes. In the glioma model that was used in this study, tumors become large heterogeneous masses, containing regions of necrosis, edema, and hemorrhage (Figure 2). The heterogeneity of the tumor region, and hemorrhage, can deteriorate local B0 homogeneity and increase linewidth. For this reason, the tumor voxel position was chosen to minimize linewidth while still containing as much tumor tissue as possible, which led to

15222594, 2022, 2, Downloaded from https://onlinelibrary.wiley.com/doi/10.1002/mrm.29243 by Cochrane Portugal, Wiley Online Library on [18/11/2022]. See the Terms and Conditions (https://onlinelibrary.wiley.com/terms-and-conditions) on Wiley Online Library for rules of use; OA articles are governed by the applicable Creative Commons License

a higher variability of voxel position in tumors and to some degree of partial volume effect in all tumor voxels. Despite all our efforts and even though the average water linewidths differences were not statistically significant, we did observe a tendency for line broadening in tumors when compared to controls that could potentially bias our results. In functional MRS for example, signals require a linewidth correction due to the very small signal difference between rest and stimulus conditions.[67–69] Future studies could attempt to decouple B0-induced line broadening from exchange-driven broadening using TE-dependent experiments and performing experiments in larger cohorts of animals. Additionally, this study does not include histopathological analysis, although the model has been extensively characterized in that regard,[70,71] including correlation with MRI,[72] and considered optimal for reproducing the histologic and immunogenic features of human glioblastoma and study new therapeutic interventions.[73] Finally, controls did not undergo surgical intervention, but this is unlikely to induce a large bias in spectral differences detected between the groups given that 3w elapsed between surgery and measurement.

From a technical perspective, it is also interesting to consider the effect of OVS radiofrequency pulses on the signal intensity of downfield resonances. Any broadband pulse followed by magnetization spoiling will potentially affect the intensity of some downfield peaks due to magnetization exchange between labile protons and water in neighboring pools. To minimize this, magnetization was excited with an adiabatic broadband sech pulse, the saturated slabs were positioned 2.5 mm away from the voxel edges to minimize spoiling "spill over" effects, and the duration of the OVS module (23 ms) was kept to a minimum. The conspicuity of peak $DF_{8.24}$-$DF_{8.49}$ in all spectra, which is almost completely suppressed by e.g. water saturation pulses,[34] suggests that the OVS module does not affect the downfield signals from exchangeable protons.

Finally, Hoefemann et al.[74] showed how the information provided by ^{1}H downfield MRS can offer further insight into the composition of the classic CEST Z-spectrum. We consider this study a first and necessary step towards informing APT and (Glu)CEST approaches and assisting their interpretation.

5 | CONCLUSION

Downfield iRE-MRS of glioma tumors revealed qualitative and quantitative spectral differences between tumor tissue and control tissue in the mouse. Given the complex factors that influence downfield spectra, including exchange, pH, microenvironments and metabolic concentrations, these findings strongly motivate future studies exploring the sources of downfield MRS signatures in cancer.

ACKNOWLEDGMENTS

This study was funded in part by the European Research Council (ERC) under the European Union's Horizon 2020 research and innovation programme (grant agreement No. 679058 - DIRECT-fMRI). The authors acknowledge the vivarium of the Champalimaud Centre for the Unknown, a facility of CONGENTO which is a research infrastructure co-financed by Lisboa Regional Operational Programme (Lisboa 2020), under the PORTUGAL 2020 Partnership Agreement through the European Regional Development Fund (ERDF) and Fundação para a Ciência e Tecnologia (Portugal), project LISBOA-01-0145-FEDER-022170. Rui V. Simões acknowledges support from H2020-MSCA-IF-2018, ref 844776.

CONFLICT OF INTEREST

None.

ORCID

Noam Shemesh https://orcid.org/0000-0001-6681-5876

REFERENCES

1. Barnholtz-Sloan JS, Ostrom QT, Cote D. Epidemiology of brain tumors. *Neurol Clin*. 2018;36:395-419.
2. Liang J, Lv X, Lu C, et al. Prognostic factors of patients with gliomas – an analysis on 335 patients with glioblastoma and other forms of gliomas. *BMC Cancer*. 2020;20:35.
3. Louis DN, Perry A, Reifenberger G, et al. The 2016 World Health Organization classification of tumors of the central nervous system: a summary. *Acta Neuropathol*. 2016;131:803-820.
4. Markopoulos GS, Roupakia E, Marcu KB, Kolettas E. Epigenetic regulation of inflammatory cytokine-induced epithelial-tomesenchymal cell transition and cancer stem cell generation. *Cell*. 2019;8:1143.
5. Korenjak M, Zavadil J. Experimental identification of cancer driver alterations in the era of pan-cancer genomics. *Cancer Sci*. 2019;110:3622-3629.
6. Hossmann KA, Mies G, Pashen W, Szabo L, Dolan E, Wechsler W. Regional metabolism of experimental brain tumors. *Acta Neuropathol*. 1986;69:139-147.
7. Mies G, Paschen W, Ebhardt G, Hossmann KA. Relationship between blood flow, glucose metabolism, protein synthesis, glucose and ATP content in experimentally-induced glioma (RG1 2.2) of rat brain. *J Neurooncol*. 1990;9:17-28.
8. Simões RV, Delgado-Goñi T, Lope-Piedrafita S, Arús C. ^{1}H-MRSI pattern perturbation in a mouse glioma: the effects of acute hyperglycemia and moderate hypothermia. *NMR Biomed*. 2010;23:23-33.
9. Thust SC, van den Bent MJ, Smits M. Pseudoprogression of brain tumors. *J Magn Reson Imaging*. 2018;48:571-589.
10. Usinskiene J, Ulyte A, Bjørnerud A, et al. Optimal differentiation of high- and low-grade glioma and metastasis: a meta-analysis of perfusion, diffusion, and spectroscopy metrics. *Neuroradiology*. 2016;58:339-350.

15222594, 2022, 2, Downloaded from https://onlinelibrary.wiley.com/doi/10.1002/mrm.29243 by Cochrane Portugal, Wiley Online Library on [18/11/2022]. See the Terms and Conditions (https://onlinelibrary.wiley.com/terms-and-conditions) on Wiley Online Library for rules of use; OA articles are governed by the applicable Creative Commons License

11. Zhou J, Heo HY, Knutsson L, van Zijl PCM, Jiang S. APT-weighted MRI: techniques, current neuro applications, and challenging issues. *J Magn Reson Imaging*. 2019;50: 347-364.
12. Ward KM, Aletras AH, Balaban RS. A new class of contrast agents for MRI based on proton chemical exchange dependent saturation transfer (CEST). *J Magn Reson*. 2000;143:79-87.
13. Cai K, Haris M, Singh A, et al. Magnetic resonance imaging of glutamate. *Nat Med*. 2012;18:302-306.
14. Cai K, Singh A, Roalf DR, et al. Mapping glutamate in subcortical brain structures using high-resolution GluCEST MRI. *NMR Biomed*. 2013;26:1278-1284.
15. Togao O, Yoshiura T, Keuppm J, et al. Amide proton transfer imaging of adult diffuse gliomas: correlation with histopathological grades. *Neuro Oncol*. 2014;16:441-448.
16. Harris RJ, Cloughesy TF, Liau LM, et al. pH-weighted molecular imaging of gliomas using amine chemical exchange saturation transfer MRI. *Neuro Oncol*. 2015;17:1514-1524.
17. Harris RJ, Cloughesy TF, Liau LM, et al. Simulation, phantom validation, and clinical evaluation of fast pH-weighted molecular imaging using amine chemical exchange saturation transfer echo planar imaging (CEST-EPI) in glioma at 3 T. *NMR Biomed*. 2016;29:1563-1576.
18. Adams B, Lerner LE. Effect of stereochemistry on hydroxyl proton chemical-shifts and coupling-constants in carbohydrates. *Magn Reson Chem*. 1994;32:225-230.
19. Govindaraju V, Young K, Mauddsley A. Proton NMR chemical shifts and coupling constants for brain metabolites. *NMR Biomed*. 2000;13:129-153.
20. Downes DP, Collins J, Lama B, et al. Characterization of brain metabolism by nuclear magnetic resonance. *ChemPhysChem*. 2019;20:216-230.
21. Piotto M, Saudek V, Sklenář V. Gradient-tailored excitation for single-quantum NMR spectroscopy of aqueous solutions. *J Biomolecular NMR*. 1992;2:661-665.
22. Dreher W, Leibfritz D. New method for the simultaneous detection of metabolites and water in localized in vivo ^{1}H nuclear magnetic resonance spectroscopy. *Magn Res Med*. 2005;54:190-195.
23. MacMillan EL, Chong DGQ, Dreher W, Henning A, Boesch C, Kreis R. Magnetization exchange with water and T1 relaxation of the downfield resonances in human brain spectra at 3.0 T. *Magn Res Med.* 2011;65:1239-1246.
24. MacMillan EL, Boesch C, Kreis R. Magnetization exchange observed in human skeletal muscle by non-water-suppressed proton magnetic resonance spectroscopy. *Magn Res Med.* 2013;70:916-924.
25. Shemesh N, Rosenberg JT, Dumez J-N, Muniz JA, Grant SC, Frydman L. Metabolic properties in stroked rats revealed by relaxation-enhanced magnetic resonance spectroscopy at ultrahigh fields. *Nat Commun*. 2014;5:4958.
26. Mori S, Eleff SM, Pilatus U, Mori N, van Zijl PC. Proton NMR spectroscopy of solvent-saturable resonances: a new approach to study pH effects in situ. *Magn Reson Med*. 1998;40: 36-42.
27. de Graaf RA, Behar KL. Detection of cerebral NAD^+ by in vivo ^{1}H NMR spectroscopy. *NMR Biomed*. 2014;27:802-809.
28. de Graaf RA, De Feyter HM, Brown PB, Nixon TW, Rothman DL, Behar KL. Detection of cerebral NAD^+ in humans at 7T. *Magn Reson Med*. 2017;78:828-835.
29. Fichtner ND, Henning A, Zoelch N, Boesch C, Kreis R. Elucidation of the downfield spectrum of human brain at 7T using multiple inversion recovery delays and echo times. *Magn Reson Med*. 2017;78:11-19.
30. Fichtner ND, Giapitzakis I-A, Avdievich N, et al. In vivo characterization of the downfield part ^{1}H MR spectra of human brain at 9.4 T: magnetization exchange with water and relation to conventionally determined metabolite content. *Magn Res Med.* 2018;79:2863-2873.
31. Borbath T, Murali-Manohar S, Wright AM, Henning A. In vivo characterization of downfield peaks at 9.4 T: T_2 relaxation times, quantification, pH estimation, and assignments. *Magn Reson Med*. 2021;85:587-600.
32. Bagga P, Hariharan H, Wilson NE, et al. Single-voxel ^{1}H MR spectroscopy of cerebral nicotinamide adenine dinucleotide (NAD^+) in humans at 7T using a 32-channel volume coil. *Magn Reson Med*. 2020;83:806-814.
33. Považan M, Schär M, Gillen J, Barker PB. Magnetic resonance spectroscopic imaging of downfield proton resonances in the human brain at 3 T. *Magn Reson Med*. 2022;87:1661-1672.
34. Gonçalves SI, Ligneul C, Shemesh N. Short echo time relaxation-enhanced MR spectroscopy reveals broad downfield resonances. *Magn Reason Med*. 2019;82:1266-1277.
35. Ordidge RJ, Connelly A, Lohman JAB. Image-selected in vivo spectroscopy (ISIS). A new technique for spatially selective NMR spectroscopy. *J Magn Reson*. 1986;66:283-294.
36. Dziadosz MBW, Doring A, Kreis R. Novel methods to record MR spectra in human brain without suppressing or exciting the water signal to investigate exchange-sensitive protons. *Proceedings of the 27th Annual Meeting of the ISMRM*. ISMRM E-Library; 2019:46.
37. Dziadosz M, Bogner W, Kreis R. Non-water-excitation MR spectroscopy techniques to explore exchanging protons in human brain at 3T. *Magn Reson Med*. 2020;84:2352-2363.
38. Simões RV, García-Martín ML, Cerdán S, Arús C. Perturbation of mouse glioma MRS pattern by induced acute hyperglycemia. *NMR Biomed*. 2008;21:251-264.
39. Pauly J, Le Roux P, Nishimura D, Macovski A. Parameter relations for the Shinnar-Le Roux selective excitation pulse design algorithm. *IEEE Trans Med Img*. 1991;10:53-65.
40. Burger C, Buchli R, McKinnon G, Meier D, Boesiger P. The impact of the ISIS experiment order on spatial contamination. *Magn Reson Med*. 1992;26:218-230.
41. Deelchand DK, Marjańska M, Hodges JS, Terpstra M. Sensitivity and specificity of human brain glutathione concentrations measured using short-TE (1)H MRS at 7 T. *NMR Biomed*. 2016;29:600-606.
42. Prinsen H, de Graaf RA, Mason GF, Pelletier D, Juchem C. Reproducibility measurement of glutathione, GABA, and glutamate: towards in vivo neurochemical profiling of multiple sclerosis with MR spectroscopy at 7T. *J Magn Reson Imaging*. 2017;45:187-198.
43. De Graaf RA. *In Vivo NMR Spectroscopy: Principles and Techniques*. John Wiley & Sons; 2019:45-50.
44. Vellido A, Romero E, Julià-Sapé M, et al. Robust discrimination of glioblastomas from metastatic brain tumors on the basis of single-voxel (1)H MRS. *NMR Biomed*. 2012;25:819-828.
45. Simões RV, Ortega-Martorell S, Delgado-Goñi T, et al. Improving the classification of brain tumors in mice with perturbation enhanced (PE)-MRSI. *Integr Biol (Camb)*. 2012;4:183-191.

15222594, 2022, 2, Downloaded from https://onlinelibrary.wiley.com/doi/10.1002/mrm.29243 by Cochrane Portugal, Wiley Online Library on [18/11/2022]. See the Terms and Conditions (https://onlinelibrary.wiley.com/terms-and-conditions) on Wiley Online Library for rules of use; OA articles are governed by the applicable Creative Commons License

46. Jiménez-Xarrié E, Davila M, Gil-Perotín S, et al. In vivo and ex vivo magnetic resonance spectroscopy of the infarct and the subventricular zone in experimental stroke. *J Cereb Blood Flow Metab*. 2015 May;35:828-834.
47. Kyathanahally SP, Mocioiu V, Pedrosa de Barros N, et al. Quality of clinical brain tumor MR spectra judged by humans and machine learning tools. *Magn Reson Med*. 2018;79:2500-2510.
48. Watanabe T, Frahm J, Michaelis T. Amide proton signals as pH indicator for in vivo MRS and MRI of the brain-responses to hypercapnia and hypothermia. *Neuroimage*. 2016;133: 390-398.
49. Pandey R, Caflisch L, Lodi A, Brenner AJ, Tiziani S. Metabolomic signature of brain cancer. *Mol Carcinog*. 2017;56:2355-2371.
50. Kong Z, Yan C, Zhu R, et al. Imaging biomarkers guided anti-angiogenic therapy for malignant gliomas. *Neuroimage Clin*. 2018;20:51-60.
51. Strauss SB, Meng A, Ebani EJ, Chiang GC. Imaging glioblastoma posttreatment: progression, pseudoprogression, pseudoresponse, radiation necrosis. *Radiol Clin North Am*. 2019;57: 1199-1216.
52. Neal A, Moffat BA, Stein JM, et al. Glutamate weighted imaging contrast in gliomas with 7 tesla magnetic resonance imaging. *Neuroimage Clin*. 2019;22:101694.
53. Sakata A, Fushimi Y, Okada T, et al. Diagnostic performance between contrast enhancement, proton MR spectroscopy, and amide proton transfer imaging in patients with brain tumors. *J Magn Reson Imaging*. 2017;46:732-739.
54. Doblas S, He T, Saunders D, et al. In vivo characterization of several rodent glioma models by 1H MRS. *NMR Biomed*. 2012;25:685-694.
55. Shemesh N, Sadan O, Melamed E, Offen D, Cohen Y. Longitudinal MRI and MRSI characterization of the quinolinic acid rat model for excitotoxicity: peculiar apparent diffusion coefficients and recovery of N-acetyl aspartate levels. *NMR Biomed*. 2010;23:196-206.
56. O'Dowd JJ, Cairns MT, Trainor M, Robins DJ, Miller DJ. Analysis of carnosine, homocarnosine, and other histidyl derivatives in rat brain. *J Neurochem*. 1990;55:446-452.
57. Braakman N, Oerther T, de Groot HJ, Alia A. High resolution localized two-dimensional MR spectroscopy in mouse brain in vivo. *Magn Reson Med*. 2008;60:449-456.
58. Lefauconnier JM, Portemer C, Chatagner F. Free amino acids and related substances in human glial tumours and in fetal brain: comparison with normal adult brain. *Brain Res*. 1976;117:105-113.
59. Zaiss M, Windschuh J, Goerke S, et al. Downfield-NOE-suppressed amide-CEST-MRI at 7 tesla provides a unique contrast in human glioblastoma. *Magn Reson Med*. 2017;77: 196-208.
60. Pan JW, Hamm JR, Rothman DL, Shulman RG. Intracellular pH in human skeletal muscle by 1H NMR. *Proc Natl Acad Sci U S A*. 1988;85:7836-7839.
61. Ray KJ, Simard MA, Larkin JR, et al. Tumor pH and protein concentration contribute to the signal of amide proton transfer magnetic resonance imaging. *Cancer Res*. 2019;79:1343-1352.
62. Khlebnikov V, van der Kemp WJM, Hoogduin H, Klomp DWJ, Prompers JJ. Analysis of chemical exchange saturation transfer contributions from brain metabolites to the Z-spectra at various field strengths and pH. *Sci Rep*. 2019;9:1089.
63. Krikken E, van der Kemp WJM, Khlebnikov V, et al. Contradiction between amide-CEST signal and pH in breast cancer explained with metabolic MRI. *NMR Biomed*. 2019;32:e4110.
64. Coman D, Huang Y, Rao JU, et al. Imaging the intratumoral-peritumoral extracellular pH gradient of gliomas. *NMR Biomed*. 2016;29:309-319.
65. Chowdhry S, Zanca C, Rajkumar U, et al. NAD metabolic dependency in cancer is shaped by gene amplification and enhancer remodelling. *Nature*. 2019;569:570-575.
66. Yaku K, Okabe K, Hikosaka K, Nakagawa T. NAD metabolism in cancer therapeutics. *Front Oncol*. 2018;8:622.
67. Mangia S, Tkác I, Gruetter R, et al. Sensitivity of single-voxel 1H-MRS in investigating the metabolism of the activated human visual cortex at 7 T. *Magn Reson Imaging*. 2006;24:343-348.
68. Schaller B, Xin L, O'Brien K, Magill AW, Gruetter R. Are glutamate and lactate increases ubiquitous to physiological activation? A (1)H functional MR spectroscopy study during motor activation in human brain at 7Tesla. *Neuroimage*. 2014;93:138-145.
69. Bednařík P, Tkáč I, Giove F, et al. Neurochemical and BOLD responses during neuronal activation measured in the human visual cortex at 7 Tesla. *J Cereb Blood Flow Metab*. 2015;35:601-610.
70. Seligman AM, Shear MJ. Studies in carcinogenesis. VIII. Experimental production of brain tumors in mice with methylcholanthrene. *Am J Cancer*. 1939;37:364-395.
71. Zagzag D, Amirnovin R, Greco MA, et al. Vascular apoptosis and involution in gliomas precede neovascularization: a novel concept for glioma growth and angiogenesis. *Lab Invest*. 2000;80:837-849.
72. Cha S, Johnson G, Wadghiri YZ, et al. Dynamic, contrast-enhanced perfusion MRI in mouse gliomas: correlation with histopathology. *Magn Reson Med*. 2003;49:848-855.
73. Oh T, Fakurnejad S, Sayegh ET, et al. Immunocompetent murine models for the study of glioblastoma immunotherapy. *J Transl Med*. 2014;12:107.
74. Hoefemann M, Döring A, Fichtner ND, Kreis R. Combining chemical exchange saturation transfer and 1 H magnetic resonance spectroscopy for simultaneous determination of metabolite concentrations and effects of magnetization exchange. *Magn Reson Med*. 2021;85:1766-1782.

SUPPORTING INFORMATION

Additional supporting information may be found in the online version of the article at the publisher's website.

Supporting Information Figure S1 Baseline fit. Illustrative example (control 2) of uncorrected spectrum (black), corrected spectrum (blue) and fit baseline (red).

Supporting Information Figure S2. In vivo iRE-MRS at short TE controls. (A), (C), (E) Voxel position in controls. (B), (D), (F) Corresponding downfield spectrum in controls. Acquisition parameters: TE = 5 ms, excitation centered at 9.5 ppm, BW = 6.5 ppm, acquisition BW = 5597.01 Hz, Number of data points = 1442, 15 repetitions. Remaining acquisition parameters as described in main text. Individual spectra aligned to $DF_{6.83}$.

15222594, 2022, 2, Downloaded from https://onlinelibrary.wiley.com/doi/10.1002/mrm.29243 by Cochrane Portugal, Wiley Online Library on [18/11/2022]. See the Terms and Conditions (https://onlinelibrary.wiley.com/terms-and-conditions) on Wiley Online Library for rules of use; OA articles are governed by the applicable Creative Commons License

Supporting Information Figure S3. In vivo iRE-MRS at short TE tumors. (A), (C), (E), (G) Voxel position in tumors. **(B), (D), (F), (H)** Corresponding downfield spectrum in controls. Individual spectra aligned to $DF_{6.83}$.

Supporting Information Figure S4. Water spectra acquired with PRESS. A) Overlay controls. **B)** Overlay tumors. **C)** Water peak fit for one illustrative control animal. **D)** Water peak fit for one illustrative tumor animal.

Note the larger inter-individual variation of the water peak area in tumors (8.9% in controls against 15.8% in tumors).

Supporting Information Figure S5. Relative metabolite peak areas (m_{AW}) calculated for individual spectra. Results for each spectral peak are presented as mean ± standard deviation calculated within each group. Statistically significant differences ($p < 0.05$) are marked with ***. All other differences had $p > 0.1$

Supporting Information Table S1 Downfield spectral peaks

How to cite this article: Gonçalves SI, Simões RV, Shemesh N. Short TE downfield magnetic resonance spectroscopy in a mouse model of brain glioma. *Magn Reson Med*. 2022;88:524-536. doi: 10.1002/mrm.29243

15222594, 2022, 2, Downloaded from https://onlinelibrary.wiley.com/doi/10.1002/mrm.29243 by Cochrane Portugal, Wiley Online Library on [18/11/2022]. See the Terms and Conditions (https://onlinelibrary.wiley.com/terms-and-conditions) on Wiley Online Library for rules of use; OA articles are governed by the applicable Creative Commons License